Frenkel pairs in low-temperature electron-irradiated InP: X-ray diffraction

K. Karsten and P. Ehrhart
Institut für Festkörperforschung des Forschungszentrums Jülich, D-52425 Jülich, Germany
(Received 12 September 1994)

Semi-insulating InP (Fe) wafers have been irradiated at 4.5 K with 2.5-MeV electrons up to a highest dose of 4×10^{19} e^-/cm^2. Without intermediate warming the irradiated samples were investigated by measurements of the change of the lattice parameter and of the diffuse scattering of x rays close to different Bragg reflections. These measurements give direct information on the structure of irradiation-induced Frenkel pairs in InP. Most characteristically, the displacement fields around interstitial atoms and vacancies must be of the same size but of the opposite sign. The separation distance of the closest Frenkel pairs is of the order of 6 Å. The introduction rate for the Frenkel pairs of $\Sigma \geq 1.5$ cm^{-1} is nearly constant up to the highest dose. Hence defect densities of $n \geq 5\times10^{19}$ cm^{-3} can be accumulated at low temperatures without indication of agglomeration or saturation. The close Frenkel pairs represent about 66% of the initial defects and anneal between 120 K and room temperature. The remaining Frenkel defects have larger distances and anneal within several annealing stages up to a highest temperature of 670 K.

I. INTRODUCTION

Point defects determine the electrical properties of semiconductors, and detailed spectroscopic data are available for many defects, especially doping atoms and complexes containing doping atoms. Much less is known about the basic intrinsic defects, i.e., the vacancies and interstitial atoms, which present a major part of technologically important defect complexes.

Pairs of interstitial atoms and vacancies (Frenkel pairs, FP's) can be produced by electron irradiation with rather high concentrations. However, similar to the observation with the elemental semiconductors Si and Ge, there is the possibility that these primary defects cannot be frozen in even at the lowest temperature due to ionization-induced migration processes, which lead to annealing and/or complexing. An additional complication with III-V compounds it the simultaneous formation of antisites and antisite complexes. Because of these complications there are many open questions concerning defect mobilities and defect reactions, even for GaAs, the best investigated III-V compound.[1–3] For InP much less is known and more detailed investigations could help to develop a general understanding of defects in III-V compounds. The present knowledge of the most basic irradiation defects in InP is based on deep-level transient spectroscopy[4–10] (DLTS) and may be briefly summarized as follows.

(i) Electron irradiation at temperatures between 15 and 300 K introduces the defect levels $E11$, $H2$, $H3$, and with the highest introduction rate of 2 cm^{-1} (for 1 MeV electrons) the level $H4$. These defect levels anneal between 340 and 420 K [annealing stage II (Refs. 4–7)]. The threshold acceleration voltage of 100 keV has been attributed to the phosphorus sublattice and corresponds to a threshold energy of $\approx$8 eV for the displacement of the P atom.[9,10] Hence these defects show a striking similarity to the 500-K annealing stage of GaAs, which has been attributed to FP's on the As sublattice. However, the details of the defect reactions lead to the conclusion that these defects must be complexes involving both irradiation defects and dopants. This conclusion means that defects on the P sublattice must be mobile during irradiation.[4] This mobility is supported by the electron paramagnetic resonance (EPR) observation of the formation of complexes around Fe dopants during irradiation at 77 K.[11]

(ii) Starting with about twice that threshold voltage for the electrons, a second group of DLTS levels can be observed. Threshold voltages between 170 (Ref. 10) and 270 keV (Ref. 9) have been reported for $H5$ and probably higher values for $E4$ and $H6$.[9] Attributing these thresholds to the displacement of In atoms yields a threshold energy between 3.5 and 6 eV for the displacement of the In atoms. As the small introduction rates[5] of 0.2 cm^{-1} are nearly two orders of magnitude below the expected values for In displacements with such a low threshold energy, this damage production is not understood and a transfer of 15–22 eV to a P atom that leads to double displacements must be considered as an alternative explanation for these higher-energy thresholds. The levels $E4$ and $H6$ anneal at temperatures between 100 and 200 K [stage I (Ref. 4)]. Such a second group of defects with higher threshold voltages, lower annealing temperature, and much lower introduction rates shows again similarities to GaAs: i.e., to the defects that are attributed to the Ga lattice. However, complexes of irradiation defects with dopants are again the most probable defect structures in InP. Hence there might be a second type of defect mobile during irradiation.

(iii) For the microscopic identification of defects positron annihilation spectroscopy (PAS), EPR, and electron-nuclear double resonance (ENDOR) have been applied. PAS yields information about vacancies as long as they are in a negative or neutral charge state and trap the positrons, and gave strong support to the attribution

0163-1829/95/51(16)/10508(12)/$06.00

of the defect annealing stages to the different sublattices in GaAs by discriminating between V_{As} and V_{Ga}.[12] After observation of the 200-K annealing stage in InP by PAS,[13] more detailed investigations[14] revealed complex reactions. For n-type InP both types of vacancies, V_{In} and V_P, are expected to be negatively charged and contribute to the positron lifetime spectrum after low-temperature irradiation. The low-temperature annealing stage is attributed to the annealing of V_{In}; hence V_P are dominating after annealing at room temperature (RT) in contrast to the conclusions obtained after RT irradiations.[15] However, a mixture of both vacancy types cannot be excluded. For semi-insulating (SI) and p-type InP, the low-temperature stage has not been observed. After annealing of SI InP to room temperature, a long lifetime is observed, which is attributed to V_{In},[14] and a similar lifetime observed after RT irradiation has been attributed to divacancies.[16] For p-type InP, V_P has been observed by EPR at RT.[17] Hence there are indications for stable vacancies on both sublattices and we might conclude that vacancies are immobile at least up to RT and the observed annealing must consequently be attributed to the mobility of the interstitial atoms. The mobility of the vacancies themselves might be deduced from the observations of the formation of vacancy agglomerates that have been reported between 420 and 570 K after e^- irradiation[15] and around 600 K after ion implantation.[18]

In addition to vacancies, the phosphorus antisite P_{In} has been identified by EPR and ENDOR.[19,20] This antisite was observed after RT irradiation; therefore it may be produced either directly by replacement collisions or by defect reactions, e.g., within the low-temperature annealing stage.

There is no direct information on interstitial atoms to our knowledge. This lack of information might be due to the fact that, as in other semiconductors, no energy level of interstitial atoms has been identified within the band gap, and interstitial atoms are therefore not accessible to most experimental methods. Hence we decided to use x-ray diffraction (XRD) techniques, i.e., measurements of the change of lattice parameter in combination with measurements of the Huang diffuse scattering (HDS). These techniques detect all defects, independent of their electronic properties, as long as they induce atomic displacement fields. In order to arrive at the simplest defect patterns, FP's were produced by electron irradiation at 4.5 K. In spite of possible ionization-induced defect migration, there might be a high chance to freeze in most of the originally produced Frenkel pairs and to observe possible low-temperature defect reactions. As it is well known that InP becomes semi-insulating after high irradiation doses[21,22] we used SI InP from the beginning in order to avoid a larger shift of the Fermi level between irradiations to different doses. Finally, we used rather high irradiation doses ($\phi t = 8\times10^{18}$–4×10^{19} electrons/cm^2) such that the concentration of irradiation-induced defects should be much higher than that of residual impurities, and intrinsic defect properties should be observed.

The high-dose approach contrasts with the electrical investigations, which show some saturation behavior due to the compensation of different defects. Although we might expect reactions at these high doses, similar investigations with GaAs (Refs. 23, 24) and preliminary results with InP (Ref. 25) showed the stability of high defect concentrations. Therefore we investigated the dose dependence of the HDS, which indicates very sensitively if defect agglomerates grow during prolonged irradiation or if saturation and/or radiation-induced annealing does occur.

In the following section we give a short introduction to the theoretical background of the methods and Sec. III summarizes some experimental details. In Sec. IV we present the experimental results, which are finally discussed in Sec. V. In a subsequent paper we will compare these results to investigations of the magnetic circular dichroism of the optical absorption.

II. THEORETICAL BACKGROUND OF THE DIFFUSE-SCATTERING TECHNIQUE

The theory of diffuse scattering from point defects in crystal is well documented[26] and we recall here those basic aspects of the scattering theory that are necessary for the understanding of the present results.

In the single-defect approximation, the scattering amplitude is represented as the sum of scattering amplitudes due to the point defects and to the distortion field around the defects:

$$S = c\left| f_D + \sum_m f_m e^{i\mathbf{k}\cdot\mathbf{r}_m}(e^{i\mathbf{k}\cdot\mathbf{s}_m} - 1)\right|^2 , \tag{1}$$

where c is the concentration of defects, f_m the atomic form factor of atom m, f_D the form factor of the defect, $\mathbf{s}_m$ the static displacement of atom m, and $\mathbf{k}$ the scattering vector. The first term, f_D, represents the scattering amplitude from the point defects (Laue scattering) and the sum describes the scattering amplitude associated with the displacements $\mathbf{s}_m$ of atoms away from their average lattice sites $\mathbf{r}_m$. As we consider only the diffuse scattering, the Bragg scattering amplitude has been subtracted in Eq. (1). The poor convergence of this lattice sum, which is due to slow $1/r^2$ decrease of the displacements, can be improved by splitting the calculation into a numerical part that considers a limited number N' of atoms that are close to the defect and have larger displacements, and an analytical approximation for the contributions from larger distances. As the displacements are very small at larger distances the exponential in Eq. (1) can be expanded, and using the lattice periodicity we obtain

$$S(\mathbf{k}) = c\left| f_D + \sum_{n=1}^{N'} f_n e^{i\mathbf{k}\cdot\mathbf{r}_n}(e^{i\mathbf{k}\cdot\mathbf{s}_n} - 1 - i\mathbf{k}\cdot\mathbf{s}_n) + \bar{f} i\mathbf{k}\cdot\tilde{\mathbf{s}}(\mathbf{q})\right|^2 . \tag{2}$$

$\mathbf{q} = \mathbf{k} - \mathbf{G}$, where $\mathbf{G}$ is the reciprocal lattice vector nearest $\mathbf{k}$.

In the approximation of the discrete lattice sum by the continuum expression for the Fourier transformation of the displacement field $\tilde{\mathbf{s}}(\mathbf{q})$, the atomic scattering factors

f_i are replaced by their average value $\bar{f}$. If there are several atoms in the unit cell this average is given by the structure factor of the unit cell, $\bar{F}$, divided by the number n_{cell} of atoms in the cell. The term $(i\mathbf{k}\cdot\mathbf{s}_n)$ is subtracted within the sum as this contribution is already contained in the analytical expression for $\mathbf{k}\cdot\mathfrak{F}(\mathbf{q})$.

The $1/r^2$ decrease of $s(\mathbf{r})$ yields a $1/q$ behavior of $\mathfrak{F}(\mathbf{q})$ and the term $\mathbf{k}\cdot\mathfrak{F}(\mathbf{q})$ is dominant close to the Bragg reflections [Eq. (2)] (Huang diffuse scattering). As the values of the Fourier transform at small $\mathbf{q}$ image the displacements at larger distance, this HDS intensity images the long-range part of the displacement field. Considering in addition only the leading term remaining after further approximations for the contributions to the sum in Eq. (2) yields

$$S(\mathbf{k})=c\,|f_D-\bar{f}(L/c)+i\bar{f}\mathbf{k}\cdot\mathfrak{F}(\mathbf{q})|^2 \tag{3}$$

with $L/c=\sum_{n=1}^{N'}(1-\cos\mathbf{k}\cdot\mathbf{s}_n)$.

L is identical to the exponent of the static Debye-Waller factor, which therefore can be determined from the diffuse scattering. For defects with large displacement fields, L is larger than f_D and L is always positive and nearly constant over the range of small $\mathbf{q}$ variations.

The next important term after $\mathbf{k}\cdot\mathfrak{F}(\mathbf{q})$ arises from the interference of L/c with this term. As L is positive the sign of this mixed term depends on the sign of the displacement field and changes with the direction of $\mathbf{q}$. This leads to an asymmetry of the HDS, comparing the scattering at $\pm q$ close to a Bragg peak (e.g., for positive $\mathbf{s}$, as is expected for interstitial atoms, the scattering at positive q will be higher than that of negative q values). From the measurements at $\pm q$ these symmetric and antisymmetric contributions can be separated and we obtain the leading term separated, i.e., the HDS in its narrow sense:

$$S_H(\mathbf{q})=[S_H(\mathbf{q}_+)+S_H(\mathbf{q}_-)]/2=c\,|\bar{f}|^2\mathbf{k}\cdot\mathfrak{F}(\mathbf{q})\ . \tag{4}$$

After determining $\mathfrak{F}(\mathbf{q})$ from Eq. (4) the Debye-Waller factor L can be determined from the antisymmetric part:

$$S_{\text{anti}}(\mathbf{q})=[S(\mathbf{q}_+)-S(\mathbf{q}_-)]/2\ . \tag{5}$$

Using elastic continuum theory we can express the long-range displacements by the dipole force tensor P_{ij} and obtain for the HDS

$$S_H=c\bar{f}^2\left[\frac{G}{q}\right]^2\frac{1}{\Omega^2}[\gamma^{(1)}\pi^{(1)}+\gamma^{(2)}\pi^{(2)}+\gamma^{(3)}\pi^{(3)}]\ . \tag{6}$$

Ω is the average atomic volume (i.e., $a^3/8$ for InP) and $\gamma^{(1)},\gamma^{(2)},\gamma^{(3)}$ are factors which depend on the elastic constants and the directions of $\mathbf{q}$ and $\mathbf{G}$. $\pi^{(1)},\pi^{(2)},\pi^{(3)}$ are quadratic expressions of the components of the dipole force tensor P_{ij} of the defects,

$$\pi^{(1)}=\tfrac{1}{3}(\mathrm{Tr}\mathbf{P})^2,\quad \pi^{(2)}=\tfrac{1}{6}\sum_{i>j}(P_{ij}-P_{jj})^2\ ,$$
$$\pi^{(3)}=\tfrac{2}{3}\sum_{i>j}P_{ij}^2\ . \tag{7}$$

By measurements in different directions of $\mathbf{q}$ and/or $\mathbf{G}$, these parameters can be determined separately.

As $\pi^{(1)}$ is proportional to the square of TrP, whereas the change of the lattice parameter is linear in c and TrP, we can determine both c and TrP by a combination of measurements of $\Delta a/a$ and S_H. From TrP we can directly deduce the relaxation volume of the defect: $V^{\text{rel}}=\mathrm{Tr}\mathbf{P}/3B$; B = bulk modulus. This value represents the volume change of the crystal due to the distortion field of one defect. The values of $\pi^{(2)}$ and $\pi^{(3)}$ determine the symmetry of the long-range displacement field of the defect; e.g., both parameters are zero for a cubic defect, $\pi^{(2)}\neq 0$ and $\pi^{(3)}=0$ for a tetragonal symmetry, $\pi^{(2)}=0$ and $\pi^{(3)}\neq 0$ for trigonal symmetry, and both parameters are $\neq 0$ for orthorhombic symmetry.

These interpretations are straightforward if there is only one type of defect; if there are, however, several defects present, the experiments yield average values. As we will consider Frenkel pairs in the following this yields

$$S_H\propto c(V_i^{\text{rel}2}+V_v^{\text{rel}2})\ \text{ and }\ \Delta a/a\propto c(V_i^{\text{rel}}+V_v^{\text{rel}})\ . \tag{8}$$

Most characteristic is that defects with opposite signs of V^{rel} can cancel in $\Delta a/a$; however, S_H depends on the square of V^{rel} and the scattering is always additive. Therefore S_H remains a measure of the changes of the defect concentrations even when $\Delta a/a$ vanishes or saturates.[24] However, additional information is necessary for a separation of the two factors c and V^{rel}.

This approach will be modified if the basic assumption of a random distribution of defects is no longer valid: Generally c must be replaced in Eq. (1) by the Fourier transform of the concentration fluctuations.[27] This yields deviations from the characteristic $1/q^2$ behavior of S_H [Eq. (6)]: e.g., for the case of defects that avoid each other, or show a tendency for ordering, we observe a decrease of the intensity at small q and for the case of clustering we observe a stronger increase at small q. For the simple model of the formation of dense clusters by the agglomeration of point defects the characteristic increase of the HDS can be quantitatively understood. If we assume that the long-range displacement fields of defects superimpose linearly upon clustering, we obtain for the scattering of a cluster of n defects

$$S(n)\simeq\frac{c_{\text{single}}}{n}(nV_{\text{single}}^{\text{rel}})^2=nc_{\text{single}}(V_{\text{single}}^{\text{rel}})^2\ , \tag{9}$$

i.e., an increase of the intensity proportional to the number of defects in the cluster. In addition, we generally observe a faster decrease of the intensity at larger values of q, i.e., $S\sim q^{-4}$.

III. EXPERIMENTAL METHODS

A. Samples and irradiations

Samples with a typical size of 5×15 mm^2 were prepared from semi-insulating [liquid-encapsulated Czochralski (LEC)] InP (2×10^{15} cm^{-3} Fe) wafers, with (100) surfaces and thicknesses $d\approx 0.5$ mm.

Irradiations were performed at a Van de Graaff accelerator with 2.5 MeV electrons using a current density of 8 μA/cm^2 while the samples were directly cooled by a stream of liquid He.[28] The irradiation dose ϕt and temperature were measured *in situ* by the change of the electrical resistivity of a copper or zinc wire that was irradi-

ated simultaneously. The samples were irradiated with doses of 0.85×10^{19}, 1.45×10^{19}, and 4.10×10^{19} e^-/cm^2, respectively. After irradiation the samples were transferred to the measuring cryostat without intermediate warming. Isochronal annealing ($\Delta t=15$ min) at each temperature was performed within the cryostat below room temperature and under vacuum ($p\leq10^{-5}$ Pa) at higher temperatures. Before the irradiations the samples had been annealed under the same conditions up to the expected highest annealing temperature of 700 K.

B. X-ray diffraction

The measurements were performed with Cu $K\alpha_1$ radiation from a 12-kW rotating-anode tube with a germanium (111) monochromator.[29,30] The lattice parameter was determined with a modified Bond technique[31] using the asymmetric (711) reflection. Diffuse scattering was measured close to the (400), (600), (511), (444), and (422) reflections; an angular region of $\pm6°$ was scanned in the ϑ-2ϑ mode with a typical step width of 0.25°. By the use of a linear-position-sensitive detector the two-dimensional intensity distribution around the reflection was determined in this way.[29] Absolute intensities were obtained by calibration with a polystyrene standard (for details, see Ref. 30). The defect-induced scattering intensity was separated from the total scattering intensity observed after irradiation by subtraction of the background that was measured before irradiation and after total annealing of the samples. This background is mainly determined by the thermal diffuse scattering, the Compton scattering, and some tails of the Bragg peak that can be assumed to be unaffected by point defects.

IV. EXPERIMENTAL RESULTS

A. Distribution of the HDS intensity

An example of the radiation-induced increase of the diffuse scattering intensity close to a (511) reflection is shown in Fig. 1. The intensity is shown along a radial direction in reciprocal space, i.e., **q** parallel to **G**. For this direction the HDS is dominated by $\pi^{(1)}$ or the trace of the dipole tensor of the defects [Eq. (6)]. The background has been measured before irradiation and there is nearly complete recovery after annealing at 740 K, except for some minor changes very close to the Bragg peak, which might also be due to some changes of the sample surface in the course of the irradiation and annealing treatments. The HDS cross section is obtained by subtraction of the background from the total scattering. Figure 2 shows examples of the observed HDS plotted as a function of the distance **q** from the corresponding reciprocal lattice vectors. For a direct comparison of the cross sections observed at different Bragg reflections, these cross sections are divided by the atomic scattering factor f (including the thermal Debye-Waller factor and polarization factors) and thus are given in atomic units; in addition the directional dependence of the leading term of the HDS [Eq. (6)] has been eliminated: $S_n=S\gamma^{(1)}(h00)/\gamma^{(1)}(hkl)$. Hence S_n is the usual

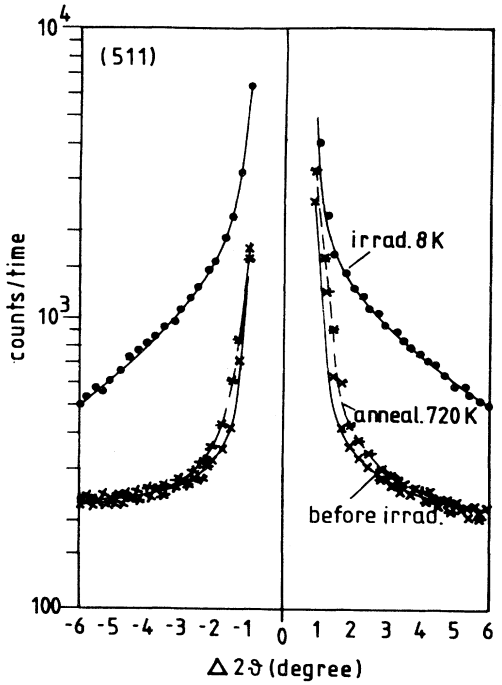

FIG. 1. Increase of the diffuse scattering intensity close to a (511) reflection in a [511] direction of q. The irradiation-induced increase of the intensity is compared to the background measured before irradiation and after annealing at 720 K. The irradiation was performed at 4.7 K to a total dose of 4.1×10^{19} e^-/cm^2.

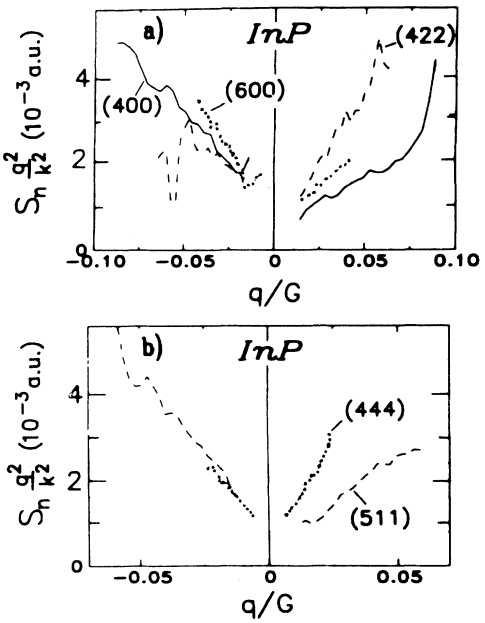

FIG. 2. Distribution of the irradiation-induced diffuse-scattering intensity ($\phi t=4\times10^{19}$ e^-/cm^2 at 4.7 K): the normalized scattering function S_n close to different Bragg reflections is shown as a function of the distance **q** from the reciprocal lattice vector **G**. The deviation vector **q** is in the radial direction in reciprocal space. (a) (400), (422), and (600) reflections; (b) (511) and (444) reflections.

scattering cross section for (400) and (600) reflections and includes a correction for other directions. Due to the multiplication of S_H with q^2 we expect a horizontal line if the scattering law [Eq. (6)] is exactly valid. Such a behavior seems to be valid after annealing above 300 K (see below), but there is a decrease of $S_H q^2$ for small values of q after irradiation. In addition we observe a large asymmetry of S_H for negative and positive deviations from the Bragg peaks. The symmetric Huang scattering S_H can directly be separated from this total scattering by taking $S^{\text{sym}}=[S(q^+)+S(q^-)]/2$ and is shown in Fig. 3. The separation of the antisymmetric scattering, however, does not remove the deviations from the q^{-2} behavior. Figure 3 shows, in addition, that these deviations seem to scale with the value of q at different Bragg reflections; such a behavior generally indicates defect correlations. The remaining antisymmetric scattering $S^{\text{asy}}=[S(q^+)-S(q^-)]/2$ is shown in Fig. 4 after multiplication with q, as we expect a q^{-1} law if this contribution is due to the interference of the Huang scattering amplitude with higher-order terms [Eq. (2)]. In contrast to the expectation for a highly distorting defect, we observe, however, a change of the sign of S^{asy} on comparing different Bragg reflections. As will be shown in Sec. V A, all these deviations from the HDS from a random distribution of defects can be consistently explained by the scattering of close FP's. Figure 5 shows the distribution of the scattering intensity around a (400) reflection. The average of $S_H q^2/G^2$ over a larger range of q is plotted against the angle ϕ between **q** and **G**. For this reflection the values of S_H at $\phi=0$ have larger errors due to a high background[29] and the values around $\phi=10$ have been used for the radial direction. $\phi=90$ corresponds to $\mathbf{q}\perp\mathbf{G}$. For this direction we expect zero intensities if the defects have cubic ($\pi^{(2)}=0$, $\tilde{\pi}^{(2)}=0$) or tetragonal ($\pi^{(3)}=0$) symmetry. Hence Fig. 5 immediately shows that the defects have a lower symmetry and the quantitative analysis shows an orthorhombic symmetry; however, this apparent symmetry might also be due to a superposition of different defects. The quantitative fit of Eq. (6) to the data, shown in Fig. 5, yields values of $\pi^{(2)}/\pi^{(1)}=0.08\pm0.01$ and $\pi^{(3)}/\pi^{(1)}=0.11\pm0.01$ for the normalized symmetry parameters. These are relatively large values for point defects; they are comparable to values expected for very anisotropic defects such as dislocation loops, e.g., an $(a/2)$ (110) loop yields $\pi^{(2)}/\pi^{(1)}=0.015$ and $\pi^{(3)}/\pi^{(1)}=0.14$ for InP.

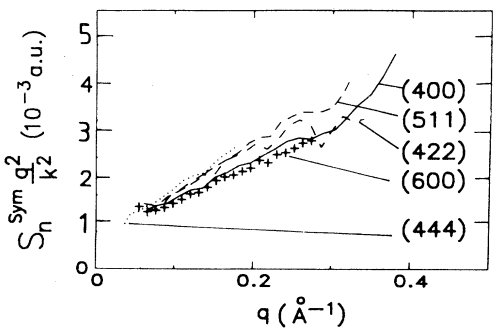

FIG. 3. Symmetrical part of the scattering function S_n shown in Fig. 2.

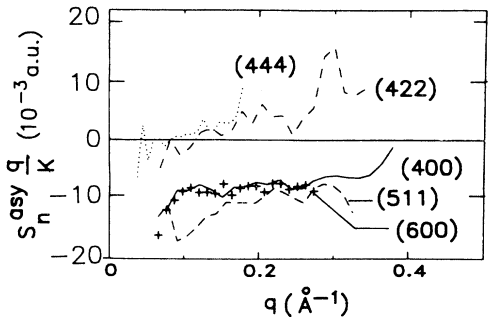

FIG. 4. Antisymmetric part of the scattering function S_n shown in Fig. 2.

B. Dose dependence of the HDS

Figure 6 shows the dose dependence of the HDS close to a (511) reflection. All the characteristic features discussed above seem to be independent of the irradiation dose and the total intensity is proportional to the dose. Similarly, the dependence of S_H on ϕ is the same for all irradiation doses (Fig. 5). Figure 7 summarizes the increase of the average intensity measured at different Bragg reflections and shows within the errors, which are characterized by the variations for different Bragg peaks, a linear increase.

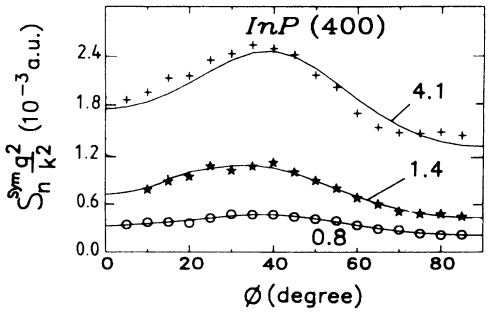

FIG. 5. Distribution of the scattering intensity around the (400) reflection of low-temperature-irradiated InP. The scattering function multiplied by q^2/k^2 has been averaged in a region of $0.1<q<0.2$ Å^{-1} and is plotted as a function of the angle ϕ between **q** and **G**; as for larger values of ϕ experimental data are available only for a smaller range of q than for $\phi\approx0$ (Fig. 3); the average has been taken consistently over this smaller range. Therefore the values for $\phi\approx0$ are about 20% lower than those discussed below (Fig. 7). By additional averaging over the four equivalent angles, the symmetric part of S_n is separated. For this (400) reflection the background for $\phi=0$ (i.e., in the radial direction and in the direction of the surface normal for a [100] crystal) is very high and purely reproducible; therefore these points are missing. The different symbols correspond to irradiation doses of 0.8×10^{19}, 1.4×10^{19}, and 4.1×10^{19} e^-/cm^2 and the solid line shows a fit of Eq. (6) to these data points that determines the symmetry parameters $\pi^{(2)}$ and $\pi^{(3)}$.

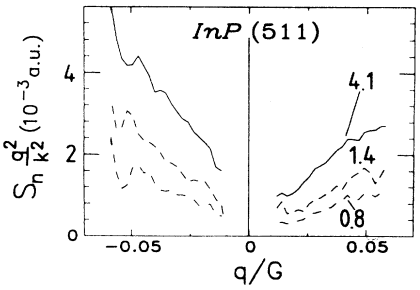

FIG. 6. Dose dependence of the irradiation-induced diffuse-scattering intensity close to a (511) Bragg reflection; as in Fig. 2 the direction of **q** is parallel to **G** (or $\phi=0$). The numbers indicate the total dose in units of 10^{19} e^-/cm^2; for better visibility the values of S_n are multiplied by a factor of 2 for the low-dose irradiations.

The figure includes also the results of the measurements of the lattice parameter: There is no change outside the error bars of 3×10^{-6} independent of the dose. Although we have a large diffuse-scattering intensity that must be due to the displacement field of defects we have no change of the lattice parameters. Hence, positive displacements, most probably by interstitials, must be nearly perfectly compensated by negative displacements, most probably by vacancies. However, due to this vanishing $\Delta a/a$, no direct separation of c and TrP is possible for InP and additional information must be used as discussed in Sec. V B.

C. Thermal annealing

The characteristic changes of the distribution of the HDS intensity on annealing are shown in Fig. 8 for the example of a (400) reflection. After annealing at 295 K the characteristic decrease of the intensity towards smaller values of q has nearly disappeared. The figure shows, in addition, that the asymmetry of the intensity has decreased during annealing to 295 K, i.e., the antisymmetric scattering contribution anneals faster than the symmetric part. After separation of the remaining antisymmetric part, the symmetric scattering $S_n^{\text{sym}}q^2$ is rather constant at 295 K. Hence deviations from the ideal HDS behavior seem to be a characteristic feature of the FP's that anneal below RT.

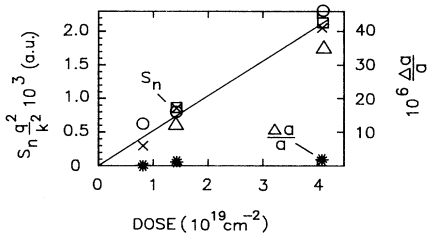

FIG. 7. Dose dependence of the average value of the symmetric part of the scattering and of the change of the lattice parameter. The averages of S_n were taken for a range of $0.1<q<0.3$ Å^{-1} (see Fig. 3). Different Bragg reflections used for the evaluation of the diffuse scattering are characterized by different symbols: ×, (400); ○, (511); □, (422); △, (444); and +, (600). The values at the (444) reflections are lower because there is only a small q range accessible ($0.08<q<0.17$).

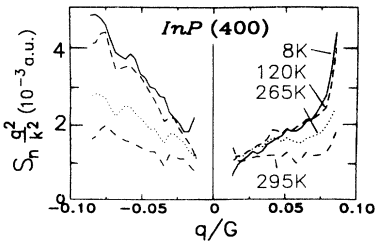

FIG. 8. Annealing of the diffuse scattering close to a (400) reflection (similar to Fig. 2) after irradiation at 4.7 K with 4×10^{19} e^-/cm^2.

The annealing of the averaged intensities is summarized in Fig. 9. These average values depend to some extent on the considered range of q, e.g., there is a faster annealing at low temperatures for large values of q than for small ones (Fig. 8). However, as we will not discuss the details of the defect distribution we have considered these differences and also the variations observed for different Bragg reflections by the error bars. Additional uncertainties arise for the low-dose irradiations due to the poorer statistics and for the medium-dose irradiation due to some instabilities of the position-sensitive detector. The main features of the annealing curves, i.e., a dominant broad annealing stage between 100 and 300 K where about $\frac{2}{3}$ of the defects anneal and a continuous further annealing up to 700 K, seem to be independent of the irradiation dose. Below room temperature we observed a faster decrease of the intensity for the low-dose irradiations; this faster decrease corresponds to a temperature shift between 30 and 70 K and indicates that more stable defect configurations are formed during prolonged

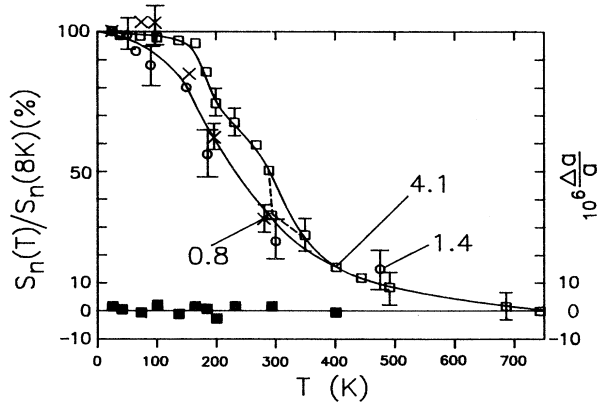

FIG. 9. Isochronal annealing (holding time=15 min) of the diffuse scattering close to a (511) reflection (average of $S_n^{\text{sym}}q^2/k^2$ for $0.017<q/k<0.053$). The different irradiation doses are indicated by the numbers in units of 10^{19} e^-/cm^2. The sample with the highest irradiation dose has been held for 8 days at RT after the first RT measurement during the isochronal annealing program. Therefore there are two data points at this temperature. The change of the lattice parameter is included for the highest irradiation dose only (full symbols), and does not show a significant change.

irradiation. For the high-dose irradiation, the broad low-temperature stage seems to be subdivided into a stage between 150 and 200 K and a second stage between 270 and 330 K.

Figure 9 shows complete annealing of the HDS at $T \approx 700$ K which is in agreement with the annealing of the lattice strain in ion-implanted InP.[32] In contrast to these observations, Fig. 1 has shown that there might be some intensity left at smaller values q; this intensity might indicate the formation of some larger and more stable agglomerates, as such clusters are characterized by a higher scattering cross section at small q [Eq. (9)] and a steeper decrease of the intensity. Such a not totally complete annealing would be in agreement with other ion and high-energy-electron irradiations;[15,18,21] however, due to the larger variations of the background at the tail of the Bragg peak, these data are not included in the quantitative discussion. In any case these surviving defects represent a minority, as the HDS, even at smaller values of q, is continuously decreasing and does not show an increase during annealing that would indicate an essential cluster growth. In addition the figure shows that there is no change in the lattice parameter within the given error bars. Also the apparent symmetry of the defects is not changed from orthorhombic as the intensity distribution shows only small quantitative changes as compared to Fig. 5.

V. DISCUSSION

The scattering cross sections discussed above represent the average scattering of vacancies and interstitial atoms on both sublattices and might include different defect complexes. For discrimination additional information is necessary and we might use the different annealing behavior as a first hint. The main question to be answered before applying the HDS theory is of course the origin of the deviation from the $1/q^2$ behavior and of the large changes in the asymmetric part of the scattering.

The decrease in the intensity could be explained as in numerous small-angle scattering experiments[33] at systems of higher concentration, by a tendency for an ordering of the defects. This ordering means that the irradiation defects repel each other such that the appearance of small interdefect distances is reduced as compared to a random distribution. For this model we would expect an increase of the effect with increasing irradiation dose. Although the dose range investigated is too small to exclude this effect definitely, there is no indication for a dose dependence in Figs. 5 and 6. Thus the correlation between the vacancy and the interstitial atom within the individual Frenkel pair and the corresponding modification of the displacement field seems to be a more appropriate explanation for the observation.

A. Structure of the Frenkel pairs

Detailed numerical simulations of the scattering intensity have been performed to explain the observed curve with the special emphasis that the model should explain also the observed changes of the asymmetry. The basic physics of the resulting defect model is shown in Fig. 10.

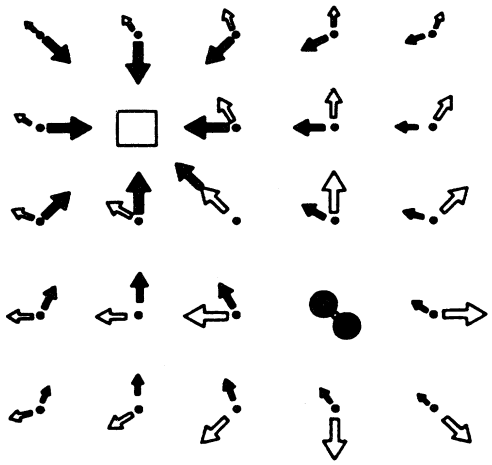

FIG. 10. Schematic view of a close Frenkel pair and the atomic displacements of the neighboring atoms. Open arrows indicate positive displacements due to an interstitial and full arrows inward relaxations due to a vacancy.

With such a FP we obtain large additive displacements between the vacancy and the interstitial and a compensation of the displacements at large distances.

In a first approach elastically isotropic displacement fields around the vacancy and the interstitial atom were superimposed:

$$\mathbf{s}(\mathbf{r}) = \frac{1}{4\pi\gamma}\left[V_i^{\mathrm{rel}}\frac{\mathbf{r}-\mathbf{R}^{\mathrm{FP}}/2}{(\mathbf{r}-\mathbf{R}^{\mathrm{FP}}/2)^3} + V_v^{\mathrm{rel}}\frac{\mathbf{r}+\mathbf{R}^{\mathrm{FP}}/2}{(\mathbf{r}+\mathbf{R}^{\mathrm{FP}}/2)^3}\right], \tag{10}$$

where γ is the Eshelby constant (a value of 1.42 has been used in the calculations), and $\mathbf{R}^{\mathrm{FP}}$ is the distance between vacancy and interstitial atom. With this displacement field the scattering was calculated using Eq. (2); the region close to the defects was calculated atomistically and for large distances the analytical approximation was used (see Ref. 30 for details). As there was a vanishing change of the lattice parameter we can assume that $V_i^{\mathrm{rel}} = -V_v^{\mathrm{rel}}$ and only one parameter is left that describes the strength of the displacements and determines the absolute scattering intensity. The remaining parameters for the calculation are the length and the direction of $\mathbf{R}^{\mathrm{FP}}$ which essentially influences the distribution of the intensity. The results of a model that reasonably reproduces the experimental observations are summarized in Fig. 11, which shows the intensity distribution in a radial direction close to different Bragg reflections. In contrast to Fig. 2 the intensity approaches zero for this calculation for a pair at a distance of $0.96a \approx 5.65$ Å. This is the expected behavior if the long-range displacements cancel completely. The value of $|q|$ where the decrease of the intensity starts to be important scales with $1/R^{\mathrm{FP}}$, hence the experimentally observed smaller slope and nonvanishing value for an extrapolation of $S(q \to 0)$ indicate a broad distribution of distances. In order to separate the more close pairs from the rest of the defects, Fig. 12 shows the experimental results if only those pairs are considered that anneal below

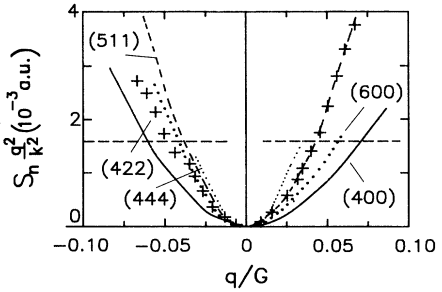

FIG. 11. Simulation of the scattering in a radial direction in reciprocal space around different Bragg reflections; the scales are identical to Fig. 2. The assumed position of the interstitial is at (0.72,0.95,0.45)a and the vacancy at (0.33,0.33,0.17)a within a cubic cell. The assumed relaxation volumes $V_i^{\mathrm{rel}} = -V_v^{\mathrm{rel}} = 0.7$ Ω. The horizontal line corresponds to the expected scattering of uncorrelated vacancy and interstitial atoms.

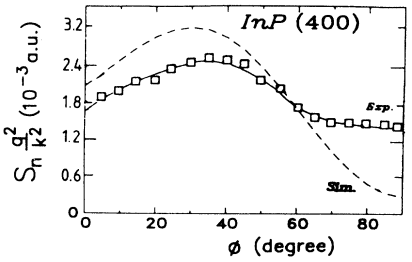

FIG. 13. Angular distribution of the scattering intensity around a (400) reflection (from Fig. 5) compared to the model calculation of a Frenkel pair. The maximum of the calculation corresponds to half the angle between **G** and the projection of the separation vector $\mathbf{R}^{\mathrm{FP}}$ of the Frenkel pair into the (110) scattering plane. The curve is obtained by averaging over the equivalent ⟨111⟩ defect axes.

RT; i.e., the total intensity at 8 K minus the remaining intensity at 295 K. This procedure yields correct values only if there is only annealing in the given temperature range and no rearrangement of the remaining defects; this assumptions seems valid here, as taking different temperature intervals (below RT) yield similar results. The good agreement of the observed intensity distributions between the simple model (Fig. 11) and the experimental result of Fig. 12 clearly supports the presence of close FP's below RT and rather well-separated FP's above this temperature (Fig. 8).

The intensity distribution around a special reflection depends on the angle between **G** and $\mathbf{R}^{\mathrm{FP}}$ and the intensity distribution calculated by the simple model is compared to the experimental results of Fig. 5 in Fig. 13. The model yields essentially a maximum at half the angle between the (100) direction and the projection of $\mathbf{R}^{\mathrm{FP}}$ into the scattering plane. Hence this distribution is determined by $\mathbf{R}^{\mathrm{FP}}$ and not only by the symmetry of the individual defects. Therefore the large values of $\pi^{(2)}$ and $\pi^{(3)}$ given above can be explained by the direction of $\mathbf{R}^{\mathrm{FP}}$ that is close to a ⟨111⟩ direction.

The exact positions of the defects additionally influence the asymmetry of S_H. Especially the observed change of the sign of S^{asy} can only be reproduced if the center of the defects is different from the highly symmetric lattice sites, because only under these conditions is there an additional phase factor between the center of the fields and the lattice sites.

Finally, the absolute intensity is mainly dependent on the size of the displacements, i.e., V^{rel}. For a given V^{rel} the defect concentration can be determined from the comparison of the absolute values of the experimental scattering function, which is proportional to $c(V^{\mathrm{rel}})^2$; the model calculation shown in Fig. 11 that fits the high-dose irradiation shown in Fig. 12 corresponds to a defect concentration of $c = 1.3 \times 10^{20}$ cm^{-3} or to an introduction rate of $\Sigma = 3.2$ cm^{-1}. In addition, these calculations show that the average intensity over the experimentally available region of q yields a value of S_H comparable to the scattering for uncorrelated defects. This can be simply understood, as the displacements are smaller at larger distances and larger at small distances (Fig. 10): i.e.,

$$S_H(q \to 0) \sim (V^{\mathrm{rel}})^2(1-1)^2$$

and (11)

$$S_H(q \to q_{\max}) \sim (V^{\mathrm{rel}})^2(1+1)^2 ,$$

where $q_{\max}$ is the value of q at which the maximum displacements are starting to dominate the scattering. Hence an average between these two values is close to the independent scattering contributions $S_H \sim 2(V^{\mathrm{rel}})^2$ and we will use in the following the standard evaluation for the averaged values of S_H, which consider the anisotropy of the displacement field.

Due to the different behavior for $q \to 0$ we can deduce the relative amount of close FP's by comparing $S_n(q \to 0)$ with the average value of S_n taken over all values of q. This estimate yields the result that about 66% of the defects are close FP's; this number agrees quite well with the amount of annealing up to RT.

In summarizing, the simple model has shown that the characteristic features of the scattering intensity can consistently be attributed to close FP's with a distance of ≈6 Å in a direction close to the ⟨111⟩ direction; these close pairs account for 66% of the defects produced at 4 K; the

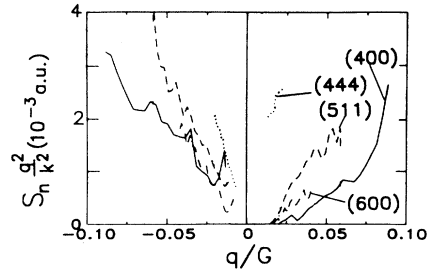

FIG. 12. Experimentally observed intensity distribution (similar to Figs. 2 and 11) by subtracting the scattering measured after annealing at 295 K from the as-irradiated intensity measured at 8 K. This intensity is assumed to correspond to the defects that anneal between 8 and 295 K.

defects remaining after annealing at RT show within the errors the scattering characteristic for randomly distributed defects. In the present state, it seems not reasonable to improve the model without having additional information as too many free parameters must be introduced, e.g., different sublattices, antisite atoms, double displacements, etc.

B. Strength and concentration of the defects

The average scattering S_H yields only a value for the product $c(V^{\rm rel})^2$ and due to the vanishing change in $\Delta a/a$ no direct separation of c and the relaxation volume $V^{\rm rel}$ is possible. Therefore we start the discussion with a plot of the interrelation between the values of c (or $\Sigma = c/\phi t$) and $V^{\rm rel}$ that are determined by the product and are shown in Fig. 14. Although there are no detailed calculations of the relaxations around defects in InP available, it seems reasonable that the lattice relaxation around a vacancy corresponds at most to $V_v^{\rm rel} = -1\Omega$. As V_i must be the same we obtain with this value a minimum value for the actual defect concentration, or more generally for the introduction rate

$$\Sigma \geq 1.5 \text{ cm}^{-1} . \tag{12}$$

This value is about 20% higher than the preliminary results[24,25] that had been obtained by averaging over a smaller range of q (similar to Fig. 5); as the simulations showed that the average over a larger range of q yields a more appropriate average, this higher value is preferred here.

As there is no theoretical lower limit for $V^{\rm rel}$ there is no definite upper limit for Σ. However, assuming that the attribution of the observed threshold voltages to the threshold energies of P and In atoms is correct, we can calculate the value of Σ,[34] i.e., a theoretical maximum for Σ or a minimum value for $V^{\rm rel}$. For the given threshold value of ≈ 8 eV for P displacements the calculated values for Σ(P) are close to the value of $\Sigma \approx 2.0$ cm^{-1} that has been observed by DLTS for the P sublattice after 1 MeV e^- irradiations,[15] and we expect a value of $\Sigma \leq 5$ cm^{-1} for our 2.5 MeV irradiation (considering multiple displacements). This introduction rate corresponds to a relaxation volume of $|V^{\rm rel}| \approx 0.5\Omega$. So far the calculation considers only the displacements of the P atoms and we have to add the introduction rate of the displacements starting at the In sublattice. An association of the higher threshold voltages (≈ 200 keV) with In displacements yields threshold energies of 3.5–6.0 eV and very high introduction rates of $\Sigma \approx 25$ cm^{-1} for our 2.5-MeV irradiations. The total introduction rate of $5+25$ cm^{-1} corresponds to $V^{\rm rel} \approx 0.2\Omega$ (Fig. 14). On the scale of $V^{\rm rel}$ we thus obtain possible values ranging from 0.2Ω to 1.0Ω which all seem reasonable as long as theory does not give a guide for a further confinement of this range. From the HDS we might deduce in addition that the smallest values of $|V^{\rm rel}|$ seem unlikely, as the observed distribution of the HDS and its fit by the model calculations indicates larger local displacements. At the other extreme, $V_v^{\rm rel} \approx -1.0\Omega$, seems very unlikely as there is no open volume left and we would not expect an observable change of the positron lifetime. Hence, a relaxation volume of $|V^{\rm rel}| \approx 0.5\Omega$ seems most reasonable and a similar value has been deduced for the vacancies in GaAs.[24]

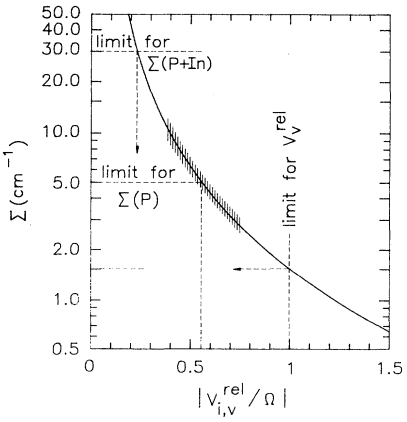

FIG. 14. Interdependence of Σ and $|V^{\rm rel}|$ as determined from the diffuse-scattering cross section [Eq. (8)] and considering that $V_i^{\rm rel} = -V_v^{\rm rel}$. An upper limit for $V^{\rm rel}$ can be assumed with $|V^{\rm rel}| = 1$ and the most reasonable values are $|V^{\rm rel}| = (0.4-0.7)$ Ω.

On the scale of the introduction rates the variation between 1.5 and 30.0 cm^{-1} is more dramatic. Again the high side of the values of Σ seems unlikely as such high introduction rates have never been observed and a value of $\Sigma \approx 5$ cm^{-1} that corresponds to $|V^{\rm rel}| \approx 0.5\Omega$ seems most reasonable. Such a value is at the limit of Σ that can be obtained if we consider only displacements starting at P atoms, even by counting all double and multiple displacements with the maximum number of surviving FP's as is done in the estimates given above. Neglecting the In displacements the threshold energies around 200 keV observed by DLTS must be attributed to these double displacements. The HDS from such events, however, needs some comments.

If the two interstitial atoms and two vacancies thus created are again locally correlated the defect model has enough free parameters to explain the scattering intensity in the same manner as for the single FP. However, the numbers refer then to the larger complex, i.e., a double FP: c is the concentration of double FP's and the total concentration of single FP's is $c_1 = 2c$ and the corresponding $|V_1^{\rm rel}| = |V^{\rm rel}|/2$; for the limiting values discussed above ($V^{\rm rel} = 1\Omega$ with $\Sigma = 1.5$ cm^{-1}) it follows that $\Sigma_1 \to 3.0$ and $|V_1^{\rm rel}| \to 0.5$. On the other hand, we might increase the absolute value of $V^{\rm rel}$ for a divacancy to 2Ω; under this condition the introduction rate is $\Sigma_1 = 0.75$ cm^{-1} in order to yield the same scattering intensity. As this maximum value for $V^{\rm rel}$ is very unlikely and only a part of the FP's will be double defects, the limiting values given above the Σ and $V^{\rm rel}$ seem reasonable considering double displacements also.

Hence we can explain all observations by primarily displaced P atoms, but the observation of the maximum Σ (including multiple displacements) is very unlikely, considering in addition that there is some defect mobility

during irradiation. Therefore we conclude that introduction rates of $\Sigma \approx 5$ cm^{-1} are reasonable only with additional displacements starting with an In atom and leading finally to a stable intrinsic defect. The annealing behavior discussed below does not reveal two stages that clearly discriminate between the two different FP's. Nevertheless, it is interesting to note that stage I is observed to be the dominating annealing stage here and not stage II, which was previously attributed to P defects and which is buried within a continuous background. If we allow for In displacements, we might also attribute one of the threshold energies around 200 keV to these displacements and we obtain a large difference between the deduced $\Sigma \approx 5$ cm^{-1} and the theoretical limit of ≈ 25 cm^{-1}. This difference indicates that a larger percentage of In FP's (as compared to P FP's) must be unstable or unstable against further irradiation. Alternatively, the assignment of the threshold energy for In displacements to values around 200 keV might be wrong, or it is also possible in principle that the threshold energy surface is very anisotropic, so that the observed minimum value is much lower than the average value observed with higher electron energies.

The exact cancellation of V_i and V_v is in contrast to GaAs but it is not a peculiarity of InP; it is observed with Si (Ref. 35) and Ge,[24,35] too. Nevertheless it seems remarkable that the large and heavy In atom induces only such small displacements. The simplest explanation, i.e., that the stable damage is mainly restricted to the P sublattice, can be excluded, as there is evidence for antisites P_{In} (Ref. 19) as well as V_{In}.[14] Also an extension of this model by the assumption that the In_i, independent of production by direct replacement or replacement collisions, finally induce a kick-out of a neighboring P atom (i.e., the final configuration would be: $V_{In}+P_i+In_P \cdots$) seems rather speculative as long as there is no direct indication of the formation of In_P. In addition, there is evidence from high-temperature Zn diffusion in InP that In_i are formed from Zn_i by a kick-out mechanism and that these In_i finally react to form dislocation loops and precipitates.[36] Hence In_i and/or their complexes with other defects seem to be characterized by rather small displacement fields.

The linear increase of S_H with the irradiation dose without indication of a saturation behavior even at high doses shows that stable defects must be produced continuously and that there are no doping atoms necessary to immobilize the defects, as this would lead to very early saturation. On the other hand, if the dopants act as unsaturable traps, a low concentration of larger defects would nucleate and we would expect a steep nonlinear increase, as is observed, e.g., for irradiated Au.[37] This cluster growth is not observed here and even at the much higher doses and dose rates within a high-voltage electron microscope no well-defined clusters are observed at irradiation temperatures below 200 °C.[38] Perfect dislocation loops, however, are observed for irradiations between 200 and 250 °C.

The observation of a very high concentration of stable FP's seems to be in contradiction to the defect mobility deduced from the trapping reactions observed by DLTS (Ref. 4) and EPR.[11] This discrepancy might be solved if we assume that the interstitial atoms have a certain probability to escape from their vacancy partner during irradiation and can be trapped at impurities; as soon as these trapping sites are occupied they may repel further defects by their Coulomb interaction. The moving interstitial atoms are retrapped at other vacancies, possibly at deeper trapping sites close to the vacancy, as these vacancies become the dominating trapping sites at higher irradiation doses.

C. Defect annealing

We have observed that $\frac{2}{3}$ of the defects anneal below RT (annealing stage I), and this annealing was attributed to the dominating recombination of close FP's. As there is general agreement that vacancies should not be mobile below RT the interstitial atoms should be the mobile species. It is remarkable, in addition, that these defects are introduced in a high concentration and are therefore the dominating defects after irradiation. There is qualitative agreement with the PAS investigations[14] that indicate the disappearance of vacancies; however, no defect densities have been published so far to our knowledge. In contrast to that, only the reactions of minority defects produced with low introduction rates have been observed within this stage by DLTS; hence these close FP's seem not to be detectable by DLTS.

Within the annealing stage II (around 370 K), which is the most prominent stage in DLTS investigations after low-dose irradiation (e.g., annealing of the levels $E11$ and $H2$–$H4$), we cannot separate a clear stage from the steady background annealing. This difference is reasonably explained as the DLTS signals are related to complexes with doping atoms, the number of which saturates at higher doses. Nevertheless, we might attribute all observations to similar defect reactions: the trapping and detrapping reactions, of probably mobile interstitial atoms, with extrinsic traps (with well-defined dissociation energies) and intrinsic radiation-induced traps (e.g., complexes with antisites, more distant FP's, di-interstitials, etc. which yield a wide spectrum of binding energies).

The annealing between 450 and 670 K leads to a nearly complete recovery of the FP's (Fig. 9). This broad annealing range, which is not resolved here in detail, has also been observed after ion and high-energy e^- irradiations, with its center located between 520 and 620 K.[18,21,32] In agreement with PAS investigations,[15,18] this stage might be attributed to the mobility of vacancies and their trapping and detrapping reactions.

Within this reaction scheme there are no annealing stages that can be definitely attributed to different defect mobilities on the two different sublattices. This observation may be understood by considering the formation of irradiation-induced antisites. For InP the P_{In} antisites have been observed,[19,20] but it is not known whether they can be formed already at the lowest threshold energy. The comparable As_{Ga} in GaAs have, however, recently been shown to be formed at energies that are believed to produce stable FP's only on the As sublattice.[39,40] This observation indicates, on the one hand, that replacement collisions might be involved in the defect formation in

III-V compounds, and, on the other hand, that the damage process for the two sublattices is no longer strictly separated. Hence the resulting FP's can no longer be attributed to one sublattice. However, further work is necessary to establish these conclusions.

VI. SUMMARY AND CONCLUSION

X-ray methods were used to investigate the properties of defects produced in InP by low-temperature electron irradiation and the defect reactions occurring during annealing up to 700 K. As it is generally observed that after high-dose irradiation InP shows semi-insulating properties, we started with SI InP so that the Fermi level is always pinned close to midgap, independent of the irradiation dose and the amount of thermal annealing. We deduced information on the location of the interstitial atoms and discussed the consequences of the observation of high concentrations of closely correlated FP's for the modeling of the behavior of radiation-induced defects in InP. Similarities to the behavior of defects in GaAs are observed and indicate general trends for the properties of irradiation defects in III-V compounds.

(i) We observed an increase of the diffuse scattering but no change of the lattice parameter and conclude that interstitial atoms and vacancies introduce lattice displacements of the same magnitude, but of opposite sign (i.e., $V_i^{\mathrm{rel}} = -V_v^{\mathrm{rel}}$; and $|V^{\mathrm{rel}}| < 1$). Similar compensations have also been observed in the elemental semiconductors Ge (Refs. 24,35) and Si;[35] however, such a small relaxation volume seems to be surprising for a large and heavy interstitial like the In atom.

(ii) The details of the scattering function can be attributed to the special structure of close FP's: a separation distance of ≈ 6 Å and a preferred orientation of the distance vector around $\langle 111 \rangle$. Very similar structures of FP's were observed for GaAs,[24,30] and also for the elemental semiconductor Ge.[24,35] These close FP's represent about $\frac{2}{3}$ of the total low-temperature-irradiation defects in InP.

(iii) We deduced a minimum introduction rate for FP's of $\Sigma \geq 1.5\ \mathrm{cm}^{-1}$, which corresponds to a maximum value of $|V_{i,v}^{\mathrm{rel}}| = 1.0\Omega$. More detailed arguments suggest a more probable value of $\Sigma \approx 5.0\ \mathrm{cm}^{-1}$ (with $|V_{i,v}^{\mathrm{rel}}| \approx 0.5\Omega$). With this high introduction rate we must assume that displacements starting from both sublattices yield stable intrinsic defects.

(iv) We observe a linear increase of the scattering intensity with the irradiation dose up to the highest dose of $4 \times 10^{19}\ e^-/\mathrm{cm}^2$. Even with the deduced minimum introduction rate $\Sigma \geq 1.5\ \mathrm{cm}^{-1}$, this corresponds to concentrations of stable FP's $\geq 5 \times 10^{19}\ \mathrm{cm}^{-3}$. From these high concentrations we deduce a quite small recombination volume for the FP's that is consistent with the small separation of ≈ 6 Å. On the other hand, the observation of stable close FP's and the missing evidence for defect agglomeration seems to be at variance with the defect mobility deduced from trapping reactions at dopants.[4] Hence we assume that interstitial atoms may escape from their vacancy; however, when all extrinsic trapping sites are occupied at higher irradiation doses the vacancies become the dominating trap and retrap interstitial atoms. Again, such a model would apply also for GaAs and Ge, where similar effects have been observed.

(v) The close FP's anneal between 120 K and room temperature; the corresponding large annealing stage I (corresponding to defect introduction rates $> 1.0\ \mathrm{cm}^{-1}$) contrasts with the DLTS results, which show only minority defect annealing below RT. Hence the close pairs seem not to be observed by DLTS; this observation is also similar to GaAs where the annealing of close FP's, which include the Ga vacancy, around RT is related only to DLTS levels of very small introduction rate.[1]

(vi) The annealing stage II (around 400 K) that is dominant in DLTS investigations is buried here under a continuous annealing background. This observation is in agreement with the attribution of stage II to detrapping from dopants. The background annealing observed here may consequently be attributed to the detrapping of the interstitial atoms from different complexes with radiation-induced antisite defects.

(vii) Within this reaction scheme it seems reasonable and in agreement with PAS results to attribute the nearly complete annealing between 450 and 670 K to the mobility of vacancies. The missing evidence for separated annealing stages for the two different sublattices can be understood by the intermixing of FP's by the formation of antisite defects along with the formation of the stable FP's.

(viii) Finally, we want to emphasize the very close similarity of the defect reactions between InP and GaAs,[24] as demonstrated by the annealing behavior of the HDS in Fig. 15. The general annealing behavior of GaAs is the same if we consider a shift of the annealing temperature by about 100 K. However, the historically developed labels of the annealing stages do not reflect this similarity; we rather have to combine the low-temperature stages I and II of GaAs and compare them to stage I of InP. Characteristically for both III-V compounds, we see a

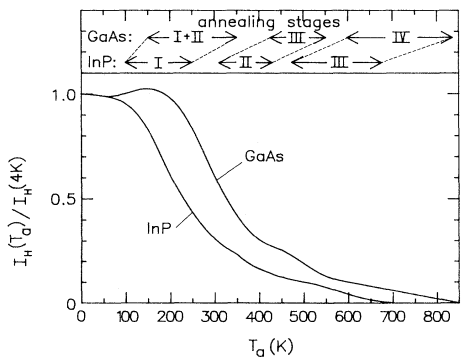

FIG. 15. Annealing of the intensity of the HDS after low-temperature electron irradiation to doses of $(1-2) \times 10^{19}\ e^-/\mathrm{cm}^2$. The similarity of InP and GaAs is obvious and after a shift by ≈ 100 K the curves are nearly identical. However, the historically evolved labels of the annealing stages do not reflect this behavior.

continuous annealing superimposed on the annealing stages that are characterized by well-defined reactions of some spectroscopically investigated defects. This behavior shows that in addition to those defects there are many additional defects and defect complexes that can rearrange and anneal. Some of these specific reactions will be investigated in a subsequent paper.

ACKNOWLEDGMENTS

The authors would like to thank Professor W. Schilling for his continuous support of this work and for many stimulating discussions. They are very grateful to Dr. Dworschak and the operating team of the Van de Graaff and to J. Koslowski for technical assistance.

[1]D. Pons and J. C. Bourgoin, J. Phys. C **18**, 3839 (1985).
[2]J. C. Bourgoin, H. J. v. Bardeleben, and D. Stiévenard, J. Appl. Phys. **64**, R65 (1988).
[3]R. C. Newman, J. Electron. Mater. **14a**, 87 (1985).
[4]A. Sibille, J. Suski, and M. Gilleron, J. Appl. Phys. **60**, 595 (1986).
[5]J. Suski, A. Sibille, and J. C. Bourgoin, Solid State Commun. **49**, 875 (1984).
[6]A. Sibille, Phys. Rev. B **35**, 3929 (1987).
[7]T. Bretagnon, G. Bastide, and M. Rouzeyre, Phys. Rev. B **41**, 1028 (1990).
[8]T. Bretagnon, G. Bastide, M. Rouzeyre, C. Delerue, and M. Lannoo, Phys. Rev. B **42**, 11 042 (1990).
[9]A. Sibille, J. Suski, and G. Le Roux, Phys. Rev. B **30**, 1119 (1989).
[10]B. Massarani and J. C. Bourgoin, Phys. Rev. B **34**, 2470 (1986).
[11]E. Y. Brailovskii, I. G. Megela, N. H. Pambuchchyan, and V. V. Teslenko, Phys. Status Solidi A **72**, K109 (1982).
[12]C. Corbel, F. Pierre, K. Saarinen, P. Hautojärvi, and P. Moser, Phys. Rev. B **45**, 3386 (1992).
[13]P. Moser, J. L. Pautrat, C. Corbel, and P. Hautojärvi, in *Positron Annihilation,* edited by P. C. Jain, R. M. Singru, and K. P. Gopinathan (World Scientific, Singapore, 1985), p. 733.
[14]M. Törnqvist, J. Nissilä, F. Kiessling, C. Corbel, K. Saarinen, A. P. Seitsonen, and P. Hautojärvi, in *Defects in Semiconductors 17,* edited by H. Heinrich and W. Jantsch, Material Science Forum Vol. 143/147 (Trans Tech, Aedermannsdorf, 1994), p. 347.
[15]V. N. Brudnyi, S. A. Vorobiev, and A. A. Tsoi, Appl. Phys. A **29**, 219 (1982).
[16]T. Bretagnon, S. Dannefaer, and D. Kerr, in *Defects in Semiconductors 16,* edited by G. Davies, G. G. DeLeo, and M. Stavola, Material Science Forum, Vol. 83/87 (Trans Tech, Aedermannsdorf, 1992), p. 1021; in *Defects in Semiconductors 17* (Ref. 14), p. 299.
[17]H. J. v. Bardeleben, Solid State Commun. **57**, 137 (1986).
[18]P. J. Schultz, P. J. Simpson, U. G. Akano, and I. V. Mitchell, in *Materials Modification by Energetic Atoms and Ions,* edited by K. S. Grabowski, S. A. Barnett, S. M. Rossnagel, and K. Wasa, MRS Symposia Proceedings No. 268 (Materials Research Society, Pittsburgh, 1992), p. 319.
[19]M. Deiri, A. Kanaah, B. C. Cavenett, T. A. Kennedy, and N. D. Wilsey, J. Phys. C **17**, L793 (1984).
[20]D. Y. Jeon, H. P. Gislason, J. F. Donegan, and G. D. Watkins, Phys. Rev. B **36**, 1324 (1987).
[21]E. Y. Brailovskii, F. K. Karapetyan, I. G. Megela, and V. P. Tartatchnik, Phys. Status Solidi A **71**, 563 (1982).
[22]K. Ando, A. Katsui, D. Y. Jeon, G. D. Watkins, and H. P. Gislason, in *Proceedings of the 15th International Conference on Defects in Semiconductors,* edited by G. Ferenczi, Materials Science Forum Vol. 38–41 (Trans Tech, Aedermannsdorf, 1989), p. 761.
[23]A. Pillukat and P. Ehrhart, in *Defects in Semiconductors 16* (Ref. 16), p. 947.
[24]P. Ehrhart, K. Karsten, and A. Pillukat, in *Beam-Solid Interactions: Fundamentals and Applications,* edited by M. A. Nastasi, L. R. Harriott, N. Herbots, and R. S. Averback, MRS Symposia Proceedings No. 279 (Materials Research Society, Pittsburgh, 1993), p. 75.
[25]K. Karsten and P. Ehrhart, in *Defects in Semiconductors 17* (Ref. 14), p. 365.
[26]P. H. Dederichs, J. Phys. F **3**, 471 (1973).
[27]M. A. Krivoglaz, *Theory of X-ray and Thermal Neutron Scattering by Real Crystals* (Plenum, New York, 1969).
[28]J. Hemmerich, W. Sassin, and W. Schilling, Z. Phys. **29**, 1 (1970).
[29]P. Ehrhart, in *Advanced Photon and Particle Techniques for the Characterization of Defects in Solids,* edited by J. B. Roberto, R. W. Carpenter, and M. C. Wittels, MRS Symposia Proceedings No. 41 (Materials Research Society, Pittsburgh, 1985), p. 13.
[30]K. Karsten, Forschungszentrum Jülich Report No. Jül 2795 (1993).
[31]W. L. Bond, Acta Crystallogr. **13**, 814 (1960).
[32]C. R. Wie, T. Jones, T. A. Tombrello, T. Vreeland, F. Xiong, Z. Zhu, G. Burns, and F. H. Dacol, in *Beam-Solid Interactions and Transient Processes,* edited by M. O. Thompson, S. T. Picraux, and J. S. Williams, MRS Symposia Proceedings No. 74 (Materials Research Society, Pittsburgh, 1987), p. 517.
[33]A. Guinier and G. Fournet, *Small Angle Scattering of X-Rays* (Wiley, New York, 1955).
[34]O. S. Oen, Oak Ridge National Laboratory Report No. ORNL-4897 (1973).
[35]S. Tietz-Hübner, Dipolma thesis, RWTH Aachen, 1993.
[36]D. Wittorf, A. Ruchi, W. Jäger, R. H. Dixon, K. Urban, H.-G. Hettwev, N. A. Stolwijk, and H. Mehrev, J. Appl. Phys. **77**, 2843 (1995).
[37]E. Segura and P. Ehrhart, Radiat. Eff. **42**, 233 (1979).
[38]F. Reynaud and B. Legros-de Mauduit, Radiat. Eff. **88**, 1 (1986).
[39]H. J. v. Bardeleben, A. Miret, H. Lim, and J. C. Bourgoin, J. Phys. C **20**, 1353 (1987).
[40]H. Hausmann (private communication).